ADVANCED ELECTRONIC MATERIALS Open Access
www.advelectronicmat.de

Controllable Laser-Induced Phase Transition in Multilayer 2H-$MoTe_2$ and its Raman Spectroscopy Study

Hao Chang, Yang Yang, Ruochen Zhang, Qinghu Bai, Xin Huang, Lingyu Wan,* and Junjie Li**

Transition metal dichalcogenides (TMDCs) heterojunctions, with their atomically precise planar structures, enable the formation of smooth and well-matched interfaces between different TMDCs components, effectively mitigating performance losses caused by lattice mismatches and rendering them highly suitable for applications in advanced devices, including 2D photodetectors, flexible light-emitting diodes, high-mobility field-effect transistors, and solar cells. Lateral heterojunctions, owing to the covalent bonding between distinct phases, demonstrate high carrier mobility, significantly lowering the contact resistance at the interface. However, the fabrication of lateral TMDCs heterojunctions is limited by several factors, including randomness, interfacial quality, and process reproducibility. In this study, a straightforward laser irradiation method for inducing phase transitions in $MoTe_2$ is presented. By optimizing the laser power and exposure duration, multilayer 2H-$MoTe_2$ encapsulated with h-BN is successfully transformed into the 1T′ phase, as verified by Raman spectroscopy. Moreover, temperature-dependent Raman spectroscopy is performed on the laser-induced 1T′-$MoTe_2$, which demonstrated the transformation into the T_d phase at ≈230K, suggesting the high structural quality of the laser-irradiated 1T′-$MoTe_2$. These results demonstrate a practical approach for phase engineering of $MoTe_2$, providing valuable insights into the fabrication of lateral heterojunctions and their future applications in high-performance photoelectric devices.

1. Introduction

2D transition metal dichalcogenides (TMDCs) have been widely studied for next-generation nanoelectronics and optoelectronics owing to their atomic-scale thickness and related striking physical and chemical properties.[1,2] TMDCs heterojunctions attributed to their unique electronic structure and the ability to tune their bandgap, are widely used as core building blocks in various cutting-edge technological fields such as flexible photodetectors, light-emitting diodes, solar cells, and next-generation field-effect transistors.[3,4] TMDCs heterojunctions can be classified as stacked and lateral heterojunctions. Controlling the interface quality between stacked TMDCs flakes is particularly challenging, potentially resulting in defects and stress concentrations that degrade the overall device performance.[5] Additionally, carrier transport in vertical structures is often restricted, reducing electron mobility and device efficiency.[2]

H. Chang, L. Wan
Center on Nanoenergy Research
Guangxi Colleges and Universities Key Laboratory of Blue Energy and Systems Integration
School of Physical Science & Technology
Guangxi University
Nanning 530004, China
E-mail: lyw2017@gxu.edu.cn

H. Chang, Y. Yang, Q. Bai, X. Huang, J. Li
Beijing National Laboratory for Condensed Matter Physics
Institute of Physics
Chinese Academy of Sciences
Beijing 100190, China
E-mail: yang.yang@iphy.ac.cn; jjli@iphy.ac.cn

R. Zhang
Laser Micro/Nano Fabrication Laboratory
School of Mechanical Engineering
Beijing Institute of Technology
Beijing 100081, China

Q. Bai, X. Huang, J. Li
School of Physical Sciences
CAS Key Laboratory of Vacuum Physics
University of Chinese Academy of Sciences
Beijing 100190, China

The ORCID identification number(s) for the author(s) of this article can be found under https://doi.org/10.1002/aelm.202500064

DOI: 10.1002/aelm.202500064

In lateral heterojunctions, domains are typically bonded through covalent bonds, in contrast to the van der Waals interactions in stacked heterojunctions.[6–8] Owing to the strong in-plane bonding between atomic layers, lateral interfaces have exhibited improved electronic performance compared with stacked (van der Waals) heterojunctions, with low resistances and high carrier mobilities, and a few orders of magnitude smaller contact area.[9,10] Covalent bonding ensures superior epitaxial quality at the interface, enhancing both electronic and thermal transport in the structure, and improving the optical and electrical properties of the heterostructure.[11,12] These advantages render lateral heterojunctions good candidates for realizing ultra-scaled contacts for truly nanoscale electronic applications.[13–15]

Chemical vapor deposition (CVD) and molecular beam epitaxy methods have been primarily used to fabricate lateral heterojunctions.[15–18] However, the sublimation and diffusion processes of reactants are difficult to control, hindering their precise fabrication.[14,19] Therefore, there is an urgent need to develop efficient and versatile fabrication strategies for lateral heterojunctions.

The polymorphism of TMDCs provides a new approach for fabricating lateral heterojunctions.[7] Molybdenum ditelluride ($MoTe_2$), a representative material within TMDCs, exhibits two stable phases (semiconducting **2H** and semi-metallic **1T′** phases) at room temperature.[20,21] The **1T′** phase can transition into the $\mathbf{T_d}$ phase between 160 K and 250 K depending on the thickness.[22–25] $\mathbf{T_d}$-$MoTe_2$, known as a type-II Weyl semimetal, exhibits superconductivity at a critical temperature and possesses topological semimetal properties, including edge supercurrent characteristics.[26–28] The energy difference between the **2H** and **1T′** phases of $MoTe_2$ is only≈43 meV per formula unit,[29] making it a highly attractive candidate for 2D phase transition planar devices.[30] Additionally, multilayer $MoTe_2$ devices demonstrate a faster optical response of 45 µs, as reported for visible light photodetectors with high optical sensitivity.[31]

Currently, several methods have been available to induce phase transitions in TMDCs such as electrostatic doping,[32] laser irradiation,[33–35]strain,[36] heavy metal doping,[37] and high-temperature annealing.[38] Electrostatic doping can induce phase transitions; however, these transitions are often reversible, meaning that the material will revert to its original phase when the electric field is removed.[39] In most strain-induced phase transitions, the phase recovers once the strain is removed.[40] In addition, excessive strain could cause cracks or defects in TMDCs, degrading their electronic and mechanical properties. In high-temperature annealing processing, high temperatures can lead to the degradation of TMDCs, thereby degrading their electronic performance. Moreover, it is difficult to produce uniform phase transitions across the entire sample via high-temperature annealing, resulting in phase mixtures that reduce the performance of the TMDCs device.[37,41–43] Heavy metal doping can induce phase instability in TMDCs, which complicates the maintenance of the desired phase. Heavy metal doping introduces numerous defects, resulting in lattice instability, as demonstrated by Raman spectroscopy.[44] Controlling the dopant concentration and distribution uniformly is still challenging.[45] Owing to the drawbacks of the fabrication methods discussed above, they are not the optimal choices for fabricating lateral heterojunctions, limiting their applications in 2D electronic and optoelectronic devices.

In summary, it is crucial to develop a method to achieve stable and regionally controllable phase transitions with reliable structural quality.

In this study, we present a reliable approach for achieving controllable and stable **2H**-to-**1T′** phase transitions in multilayer $MoTe_2$ via laser irradiation. Through the precise control of the laser irradiation time, a uniform and high-quality **1T′** phase was successfully induced in multilayer **2H**-$MoTe_2$. Temperature-dependent Raman spectroscopy further confirmed the laser-induced **1T′**-to-$\mathbf{T_d}$ phase transition, as evidenced by the characteristic splitting of Raman peaks, indicating the high lattice quality of laser-processed samples. Furthermore, systematic Raman analysis of multilayer $MoTe_2$ subjected to different laser irradiation durations revealed a transition from a pure **1T′** phase to a mixed phase consisting of both **1T′** and impurity phases. Notably, as the irradiation time increased, the phase transition temperature decreased, which is attributed to the formation of tellurium (Te) clusters. These clusters are likely to introduce lattice distortions, thereby hindering the transition to the $\mathbf{T_d}$ phase. This study provides new insights into the laser-induced phase engineering of $MoTe_2$ and offers a scalable strategy for achieving precise and stable phase transitions in layered TMDCs.

2. Results and Discussion

Each $MoTe_2$ layer was composed of three hexagonal units, with a thickness of ≈6–7 Å, forming a trilateral structure with a chemical composition of Te-Mo-Te. The metal (Mo) layer was sandwiched between two layers of Te atoms in a trigonal prismatic arrangement exhibiting strong covalent bonds, whereas the adjacent layers were held together by weak van der Waals forces. Owing to differences in stacking and lattice distortions, $MoTe_2$ exhibits two configurations—trigonal prismatic (**2H**) and monoclinic (**1T′**) phases—at room temperature, as illustrated in **Figure 1a,b**.[28] Figure 1c presents the schematic structure of the sample and fabrication process. The bottom purple layer represents SiO_2, the middle atomic layer corresponds to **2H**-$MoTe_2$, and the top transparent layer is **h**-BN, which provides protection. The laser-ablated region is indicated by a white square area in the figure. Figure 1d shows an optical microscope image of the laser-ablated multilayer **2H**-$MoTe_2$, which was previously covered with **h**-BN. The **h**-BN layer is highlighted within the orange polygonal frame, and the **2H**-$MoTe_2$ layer lies underneath it. The thickness of the multilayer **2H**-$MoTe_2$/**h**-BN structure was measured using atomic force microscopy, as shown in Figure S1 (Supporting Information). The results show that the $MoTe_2$ flake had a thickness of ≈10 nm (corresponding to≈14 layers) and that the **h**-BN substrate had a thickness of 5 nm, resulting in a total stacked thickness of ≈15 nm. The red boxes indicate the laser ablation areas, which measure 100 μm^2.

Figure 1e shows the Raman spectra of different $MoTe_2$ samples. The Raman spectrum of **h**-BN-encapsulated **2H**-$MoTe_2$ is indicated by the green line in Figure 1e, in which the distinct vibrational modes at 171 cm^{-1} (A_{1g} mode), 235 cm^{-1} (E^1_{2g} mode), and 290 cm^{-1} (A^2_{1g} mode) can be clearly observed. This spectrum fully resumes the spectral characteristics of **2H**-$MoTe_2$, as reported in previous literatures,[31,46] confirming the quality of **h**-BN encapsulation around **2H**-$MoTe_2$ in this study. The

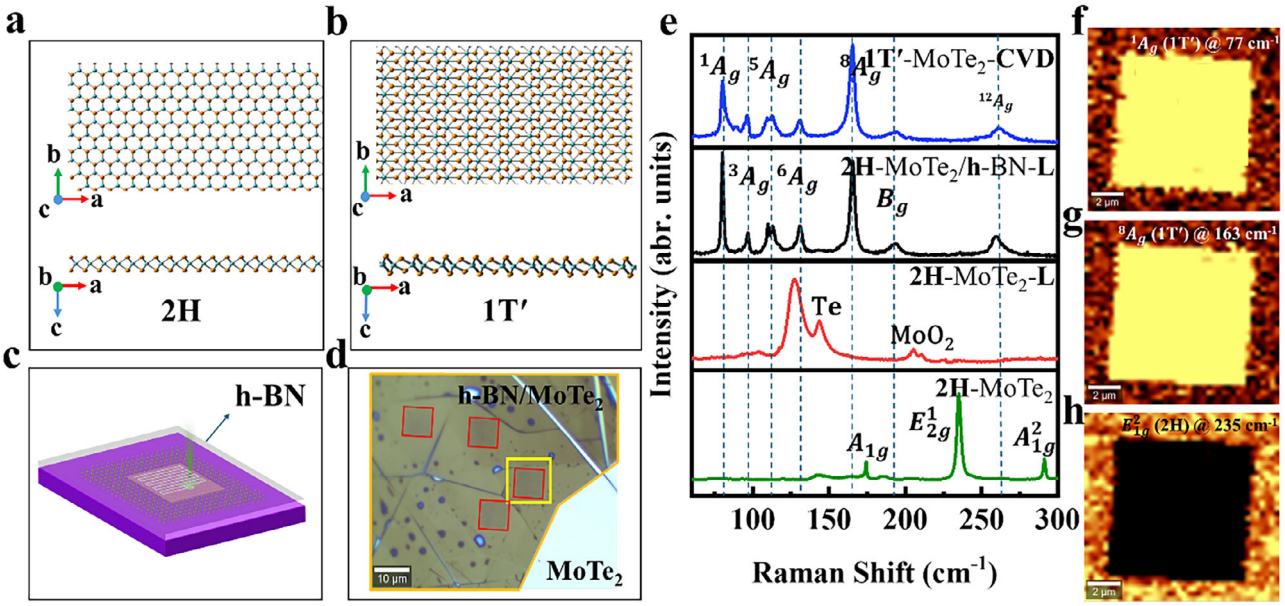

Figure 1. Atomic structure models of a) 2H- and b) 1T′-$MoTe_2$ with top and side views. Monolayer models are created for clarity. c) Schematic diagram of the 2H-$MoTe_2$ flake structure encapsulated by the h-BN layer, and the laser ablation process on the structure. d) Optical microscope image of the h-BN covered multilayer 2H-$MoTe_2$ after laser ablation (red box). e) Raman spectra of the pristine 2H-phase $MoTe_2$ (green line), the laser-processed 2H-$MoTe_2$ (red line), the laser-processed h-BN covered with 2H-$MoTe_2$ (black line), and the CVD-grown 1T′-$MoTe_2$ (blue line). f) Raman mapping image created using the intensity of the ^1A_g peak at 77 cm^{-1} of 1T′-$MoTe_2$. g) Raman mapping image created using the intensity of the ^8A_g peak at 163 cm^{-1} of 1T′-$MoTe_2$. h) Raman mapping image created using the intensity of the E^1_{2g} peak at 235 cm^{-1} of 2H-$MoTe_2$.

Raman peak at ≈290 cm^{-1} was designated as the A^2_{1g} peak, with a stronger peak indicating that the sample is very thin.[47,48] The red line in Figure 1e represents the laser-ablated bare **2H**-$MoTe_2$, named as **2H**-$MoTe_2$-L. The peaks at 125 and 140 cm^{-1} were designated as A_g and E_g modes of **1T′**-$MoTe_2$, respectively.[33] However, recent studies suggested that these two Raman peaks for the laser-ablated $MoTe_2$ could be attributed to the presence of Te clusters.[49] This is the most common phenomenon observed in previous laser ablation studies.[30,50,51] The Raman peak at 200 cm^{-1} is attributed to the formation of MoO_2, indicating that laser ablation in air results in the oxidative decomposition of $MoTe_2$. Although the 200-cm^{-1} peak has been attributed as the B_g mode of **1T′**-$MoTe_2$ in some previous studies,[49] our systematic analysis revealed this feature to be unambiguously associated with MoO_2. As shown in Figure 1, the intrinsic B_g mode of phase-pure **1T′**-$MoTe_2$ exhibited a stable characteristic peak at 191 cm^{-1}, consistently observed in both laser-ablated **h**-BN-encapsulated **2H**-$MoTe_2$ and pristine CVD-grown **1T′**-$MoTe_2$. In addition, we expanded the spectral analysis to 1500 cm^{-1} (Figure S2, Supporting Information). The extended dataset clearly exhibited two peaks in **2H**-$MoTe_2$-L, located at 200 and 750 cm^{-1}, which align with the MoO_2 peaks reported in the literatures.[52,53] Therefore, our systematic analysis revealed 200 cm^{-1} peak to be unambiguously associated with MoO_2. These spectral characteristics of **2H**-$MoTe_2$-L confirmed that laser processing under ambient conditions introduced structural defects (Te vacancies) and spontaneous MoO_2 into $MoTe_2$. It is well known that covering with **h**-BN is a common method to protect 2D materials from ablation.[50,51] Ryu Huije et al. has reported the pure **1T′**-$MoTe_2$ phase using the sandwich structure of **h**-BN/$MoTe_2$/**h**-BN.[51] However, this fabrication process is slightly complicated. These observations motivated our investigation of **h**-BN encapsulation methods.

A complete **2H** to **1T′** phase transition was realized by covering **h**-BN on the top of **2H**-$MoTe_2$ (**2H**-$MoTe_2$/**h**-BN-L), as illustrated by the black line in Figure 1e. Notably, by comparing with the Raman characteristic peaks of a standard **1T′** sample created using CVD (blue line), the Raman spectrum of **2H**-$MoTe_2$/**h**-BN-L had the same Raman spectroscopic features of **1T′** phase $MoTe_2$, confirming that the laser-ablated **h**-BN-encapsulated $MoTe_2$ could hold a high-quality **1T′** phase. As indicated by the top two black and blue lines in Figure 1e, all seven prominent Raman peaks of **1T′**-$MoTe_2$ were observed within the range of 77–259 cm^{-1}. The peak at 77, 90, 111, 124, 163, and 259 cm^{-1} was designated as A_g mode and that at 193 cm^{-1} was designated as B_g mode, which indicate the presence of the **1T′** phase.[49] In previous studies of voltage-induced phase transitions, the peak at 163 cm^{-1}, labeled as ^8A_g, was typically used as a benchmark for identifying the **1T′** phase.[37] However, in previous laser ablation experiments on **h**-BN-covered $MoTe_2$, the ^8A_g peak or other **1T′** characteristic peaks were not detected, suggesting that these may be signals from Te clusters.[49] Wang et al.[32,54] reported similar findings that the disappearance of A_{1g} and E^1_{2g} modes was accompanied by the appearance of a new Raman peak at ≈163 cm^{-1}, identified as the ^8A_g mode in **1T′**-$MoTe_2$. To assess whether the sample was thinned by the laser, we measured the Raman intensity of the Si substrate from both the ablated and nonablated regions. The intensity difference of the Raman peak of the Si substrate at 520 cm^{-1} before and after laser irradiation remained below 5%, which was

significantly smaller than the intensity change caused by a single-layer thickness (≈25%), confirming that the laser parameters were rigorously maintained below the laser thinning threshold. Detailed information is provided in Figure S3 (Supporting Information). Under the same laser parameters, ablation experiments were conducted on bulk **2H**-$MoTe_2$ (thickness, 300 nm; Figure S4, Supporting Information). The Raman spectra confirmed the formation of a coexisting state of the **1T′** phase (163 cm^{-1}) and the **2H** phase (235 cm^{-1}) in the bulk sample (Figure S5, Supporting Information). This behavior is consistent with the phase transition threshold observed in multilayer samples, suggesting that controlled phase transitions can be achieved in thick samples under the same energy density.

Previous studies have shown that the thermal effect plays a key role in the laser-induced **2H**-to-**1T′** phase transition.[55–57] During laser ablation, energy is converted into the lattice thermal energy via electron–phonon coupling, leading to localized temperature accumulation.[51,58] In addition, the laser-ablated **2H**-$MoTe_2$/**h**-BN remained stable in the standard **1T′** phase under ambient conditions even after 1 month (Figure S6, Supporting Information).

To investigate the uniformity and quality of laser-induced **1T′** phase $MoTe_2$, Raman mapping was performed on the laser-ablated zone of $MoTe_2$, which is highlighted by the yellow box in Figure 1d. In Figure 1f, the ^1A_g peak intensity at 77 cm^{-1}, corresponding to the **1T′**-$MoTe_2$ phase, is presented. A strong Raman signal was observed within the laser-processed area, indicating that the **1T′** phase formed because of laser ablation. This clear signal highlights the successful phase transition from the original phase to **1T′**-$MoTe_2$. Similarly, Figure 1g shows ^8A_g at 163 cm^{-1}, another characteristic mode of **1T′**-$MoTe_2$. A prominent Raman signal was detected in the ablated region, with the mapped area visually represented in yellow. The consistency between Figure 1f,g reinforces the conclusion that laser processing induced a reliable and uniform phase transition to **1T′**-$MoTe_2$ across the treated area. Figure 1h shows the Raman mapping constructed using the peak at 235 cm^{-1} (E^1_{2g}), which is the characteristic peak of the **2H**-$MoTe_2$ phase. The laser-ablated region appears black, signifying the absence of the **2H**-$MoTe_2$ within this area. The lack of a Raman signal at 235 cm^{-1} confirms that no residual **2H**-$MoTe_2$ was detected in the processed region. The observations in Figure 1f—h indicate that the **2H** phase was completely converted to the **1T′** phase during the laser ablation process, demonstrating the uniformity and controllability of the method proposed in this study, each representing a region of perfect **1T′** phase transition induced by laser ablation. This indicates that laser ablation allows for precise control over the transition regions, including their location, size, and uniformity, and could be a candidate for fabricating lateral heterojunctions.

It is well known that the standard **1T′**-$MoTe_2$ undergoes ^6A_g peak splitting at low temperatures, indicating the transition from **1T′** to $\mathbf{T_d}$ phase.[32,59] By performing low-temperature Raman spectroscopy, we evaluated the quality of the laser-induced **1T′**-$MoTe_2$ sample in this study. **Figure 2a** shows the temperature-dependent Raman spectra of **2H**-$MoTe_2$/**h**-BN-L. The Raman spectrum at 300 K assumed the typical characteristics of **1T′**-$MoTe_2$. The overall trend indicates that all Raman peaks shifted

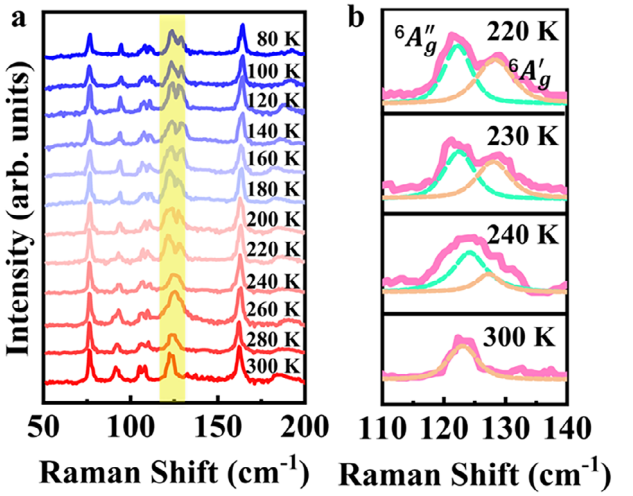

Figure 2. a) Temperature-dependent Raman spectra of 2H-$MoTe_2$/h-BN-L. b) Raman spectra that are collected at selected temperatures of 220, 230, 240, and 300K and processed with peak fitting.

toward higher frequencies as the temperature decreased. Notably, the ^6A_g peak exhibited prominent changes in the yellow-highlighted region, as shown in Figure 2a. Only a distinctive ^6A_g peak was observed in the range of 300–240K. However, as the temperature decreased, the ^6A_g peak began to split at ≈240K, and two clear peaks were observed at 220K and lower temperatures. The detailed evolution of the ^6A_g mode is shown in Figure 2b, which was fitted using the Gaussian–Lorentzian functions. As shown in Figure 2b, as the temperature decreased, at 230 K, the ^6A_g Raman peak of the laser-processed **1T′** sample split on the left side, with the resulting peak labeled as $^6A''_g$. However, as the temperature decreased, the $^6A'_g$ peak became increasingly prominent. Therefore, Raman peaks progressively shifted with decreasing temperature, and this change became more pronounced at lower temperatures.[60] The two Raman peaks, identified from the ^6A_g fitting of $\mathbf{T_d}$-$MoTe_2$, were designated as $^6A'_g$ and $^6A''_g$ to enable a more accurate extraction of characteristic parameters from the spectral peaks. In **Figure 3b**, the peak on the left corresponds to the $^6A''_g$ mode, whereas that on the right represents the $^6A'_g$ mode. The intensity variation was observed at ≈230 K, demonstrating the transition characteristics from the **1T′** phase to the $\mathbf{T_d}$ phase, which is consistent with that reported in previous studies.[22,61] Compared with the results reported by Kowalczyk,[49] the phase transition temperature in the present study marginally increased. The difference in the phase transition temperature can be attributed to the adoption of the **h**-BN encapsulation layer. Owing to the thermal insulation properties of **h**-BN, which effectively suppress heat dissipation, the phase transition temperature in **h**-BN-coated **1T′**-$MoTe_2$ was elevated compared with that of **1T′**-$MoTe_2$ without **h**-BN encapsulation.[62]

Figure 3a shows the Raman spectra of **h**-BN-covered $MoTe_2$ samples subjected to different laser ablation times. We found that the critical ablation time was 1 s, where the Raman spectrum perfectly matched the spectrum of the ideal **1T′**-$MoTe_2$ phase shown in Figure 1e. As the laser ablation time increased, the Raman peaks originating from Te clusters gradually appeared at 124 and

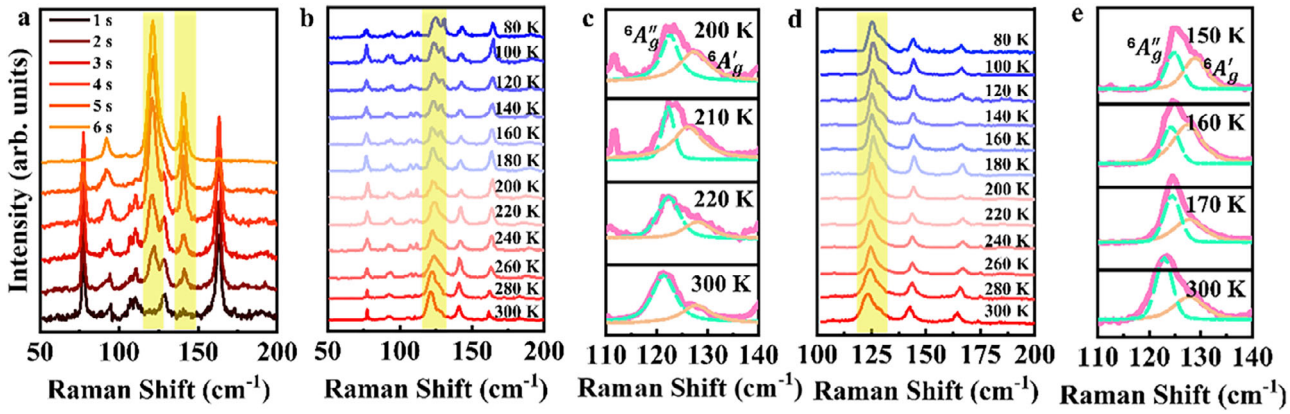

Figure 3. a) Raman spectra of h-BN-covered 2H-$MoTe_2$ under different ablation times. b) Temperature-dependent Raman spectra of 2H-$MoTe_2$/h-BN-L under a laser ablation duration of 4 s. c) Fitted Raman spectra measured at selected temperatures of 200, 210, 220, and 300 K shown in b). d) Temperature-dependent Raman spectra of 2H-$MoTe_2$/h-BN-L under a laser ablation duration of 6 s. e) Fitted Raman spectra measured at selected temperatures of 150, 160, 170, and 300K shown in d).

141 cm^{-1}, as highlighted in the in yellow box. Specifically, the Raman peak at 124 cm^{-1} became significantly stronger, and a new peak emerged at 141 cm^{-1}.[38,49] Although **h**-BN encapsulation can effectively protect **2H**-$MoTe_2$ from oxidation, it does not suppress the formation of Te clusters under certain conditions. The formation of Te clusters is a well-known phenomenon that occurs on the surface of Te-containing materials with inherent instability.[63,64] Te is a mobile species that easily migrates and clusters at relatively high temperatures. Therefore, with increased laser irradiation, localized thermal accumulation induces the formation of Te clusters.[49] At 6 s, the ^8A_g peak at ~163 cm^{-1} completely disappeared, indicating a deterioration in the crystal structure of the **1T′**-phase $MoTe_2$.[65–68] To further investigate whether the lattice quality is truly affected, we selected the samples with 4-s (**2H**-$MoTe_2$/**h**-BN-L 4 s) and 6-s (**2H**-$MoTe_2$/**h**-BN-L 6 s) ablation times to study the phase evolution at low temperatures. Temperature is an indication of thermal effects from laser ablation and is critical for evaluating the thermal driving force of the **2H**-to-**1T′** phase transition. The temperature of the laser-ablated region was estimated using the intensity ratio of the Anti-Stokes/Stokes Raman peaks.[69]

The intensity ratio between the Anti-Stokes (energy gain) and Stokes (energy loss) peaks was governed by the Boltzmann distribution as follows:

$$\frac{I_{Anti-Stokes}}{I_{Stokes}} = \left(\frac{\omega_0 + \omega}{\omega_0 - \omega}\right)^4 e^{-\hbar\omega/(k_B T)} \quad (1)$$

where ω_0 is the incident laser frequency, ω is the phonon frequency, k_B is the Boltzmann constant, $\hbar$ is the reduced Planck constant, and T is the temperature. In this study, ω_0 was set to 532 nm, and ω was set to 163 cm^{-1} for **2H**-$MoTe_2$/**h**-BN-L 1S and 121 cm^{-1} for **2H**-$MoTe_2$/**h**-BN-L 3S, respectively. The temperature for **2H**-$MoTe_2$/**h**-BN-L 1S was 752 K, whereas that for **2H**-$MoTe_2$/**h**-BN-L 3S reached 1021K. (Figure S7 and Note S1, Supporting Information). These results align with those of previous literatures.[34,55] A pure **2H**-to-**1T′** phase transition occurred at a relative low temperature, whereas a mixed phase of Te clusters and the **1T′** phase emerged as the temperature increased.[33,51]

Figure 3b presents the Raman spectra of the multilayer **1T′**-$MoTe_2$ laser-ablated area, where the laser ablation duration was 4 s (**2H**-$MoTe_2$/**h**-BN-L 4 s) with **h**-BN.[32,59] These features were attributed to Raman peaks induced by Te clusters. Figure 3c shows a clearer image of the temperature points selected before and after the phase transition in Figure 3b. The peak on the left corresponds to the $^6A''_g$ mode, whereas that on the right represents the $^6A'_g$ mode. The intensity variation was observed at ≈210K, consistent with the transition characteristics from the **1T′** phase to the $\mathbf{T_d}$ phase.

Figure 3d shows the Raman spectra of the multilayer **1T′**-$MoTe_2$ region after 6 s of laser ablation with **h**-BN encapsulation. The temperature-dependent Raman spectra in Figure 3b revealed that, at ≈160K, a shoulder peak appeared on the right side of the ^6A_g Raman peak. As shown in Figure 3e, a similar Raman peak-fitting analysis for the ^6A_g mode was performed for the sample subjected to 6 s of laser ablation. The results showed that, at temperatures of 170K and above, the intensity of the $^6A'_g$ peak remained relatively low. However, a notable increase in intensity was observed at 160K. **Figure** 4c shows the temperature-dependent intensity ratio of $^6A'_g$ and $^6A''_g$ peaks. The intensity variation of these two peaks observed at ≈160K signified the characteristic phase transition from **1T′** to $\mathbf{T_d}$. This indicates the occurrence of a phase transition.

To provide a more compelling evidence for the low-temperature phase transition in our sample, a comprehensive analysis of the evolution of the peak-splitting intensity of the ^6A_g mode is presented in Figure 2a. Extensive literature supports the observation that, during the phase transition from the **1T′** phase to the $\mathbf{T_d}$ phase, the ^6A_g mode undergoes significant splitting, resulting in the formation of two distinct peaks.[22,49] The intensity ratio between the two component peaks, $^6A'_g$ and $^6A''_g$, that make up the fitted ^6A_g mode. By tracking the changes in the relative intensity of these two component peaks, the occurrence of **1T′** to $\mathbf{T_d}$ phase transition could be clearly identified. The intensity ratio between these two component peaks served as a critical parameter for evaluating the relative strengths of the split peaks. Figure 4a shows the fitted relative intensity ratios of these two peaks over the temperature range of 300–80K for **2H**-$MoTe_2$/**h**-BN-L 1 s,

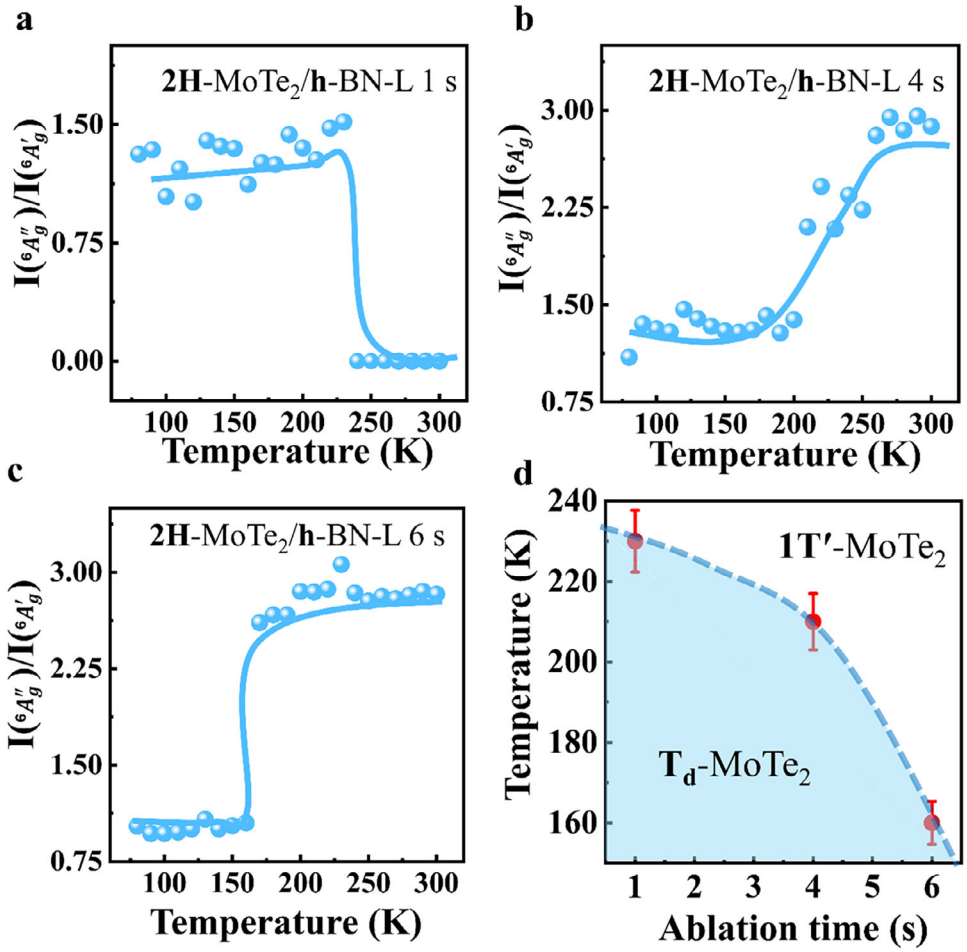

Figure 4. a–c) Intensity ratio of $^6A'_g$ and $^6A''_g$ for 2H-$MoTe_2$/h-BN-L 1 s at 4 and 6 s, respectively. d) Phase diagram of **1T′** and $\mathbf{T_d}$ phases as a function of temperature and laser ablation time, with T_d represented in blue.

with the corresponding results plotted. Notably, a sudden change in the intensity ratio occurred at ≈230K, where the intensity of the $^6A'_g$ peak increased. Specifically, the relative intensity ratio between the two peaks increased to 1.5. This sharp rise in intensity strongly suggests the phase transition of the **1T′** to $\mathbf{T_d}$. This provides compelling evidence that the phase transition occurs at ≈230K in **2H**-$MoTe_2$/**h**-BN-L 1 s. However, in the 4-s laser ablation experiments shown in Figure 4b, the lattice structure was affected due to laser scanning during the **1T′** phase–induced phase transition, resulting in an increase in the number of Te clusters, and a clear splitting of the ^6A_g mode was observed. Despite this, we accurately quantified the intensity ratio between the two component peaks—$^6A'_g$ and $^6A''_g$ over a temperature range from 300 K to 80 K and plotted the results. One noteworthy observation in the data is the sudden change in the intensity ratio at ≈210K. The intensity of the $^6A'_g$ peak showed a significant increase, with the relative intensity ratio between the two peaks decreasing from ≈2.8 to 1.2. This change corresponds to a 60% reduction in the intensity of the $^6A''_g$ peak relative to the $^6A'_g$ peak. This sharp reduction in intensity strongly suggests the phase transition of the **1T′** phase to the $\mathbf{T_d}$ phase. This provides compelling evidence that a phase transition occurred in the 4-s laser multilayer sample at ≈210K. Figure 4c illustrates the temperature-dependent peak intensity of $^6A'_g$ and $^6A''_g$ modes in the 6-s laser-ablated $MoTe_2$ sample. Temperature-dependent experiments ranged from 300 to 80K, allowing us to clearly observe the abrupt change in the $^6A'_g$ intensity. As shown in figure, the intensity ratio of $^6A''_g$ to $^6A'_g$ decreased from 3.0 to 1.0 at ≈160K, representing a 200% reduction. This corresponds to doubling of the $^6A'_g$ intensity compared with its initial value. These findings suggest that a structural phase transition occurred in the 6-s laser-ablated sample at ≈160K.[70] By extracting the laser ablation time and phase transition temperature information from Figure 4a–c, a functional relationship between the laser ablation time and the phase transition temperature was obtained. The time-temperature phase transition diagram of $MoTe_2$ is shown in Figure 4d. in which the white to blue area clearly shows the dynamic transformation from the **1T′** phase to the $\mathbf{T_d}$ phase. The red circular data points represent the temperatures at which the phase transitions occurred at the laser ablation times in this experiment. The dashed blue curve represents the fitted boundary separating the stability regions of the two phases. The upper region above the curve corresponds to the stability range of the high-temperature **1T′**-$MoTe_2$ phase, and the shaded blue area below the curve corresponds to

the stability range of the low-temperature $\mathbf{T_d}$-$MoTe_2$ phase. Notably, the phase transition temperature decreased with increasing ablation duration. This phenomenon can be attributed to the increase in the number of Te clusters in the ablated $MoTe_2$, as previously reported.[49] As shown in Figure 3a, as the laser irradiation time increased, the sample gradually transformed from a pure **1T′** phase to a mixed phase consisting of Te clusters and the **1T′** phase. Consequently, local lattice distortions and Te vacancies were continuously formed during the formation of Te clusters, creating energy barriers that hinder the cooperative atomic rearrangement required for structural transitions, leading to a reduced phase transition temperature.[63,71]

3. Conclusion

In conclusion, we proposed a method for the controllable and stable fabrication of a lateral heterostructure in the multilayer $MoTe_2$. By optimizing the laser ablation power and time, a uniform and high-quality transition from the **2H** phase $MoTe_2$ to the **1T′** phase $MoTe_2$ was successfully achieved, and their structural properties were systematically investigated using temperature-dependent Raman spectroscopy. The **1T′**-to-$\mathbf{T_d}$ phase transition at 230K became distinctly evident in the multilayer **2H**-$MoTe_2$ samples subjected to laser ablation of 1 s. The analysis of Raman spectra revealed the complete phase transition pathway, including the transitions from **2H** to **1T′**, followed by the coexistence of **1T′** and Te clusters. Additionally, temperature-dependent Raman measurements were employed to investigate the phase transition from **1T′** to $\mathbf{T_d}$ in $MoTe_2$ with mixed Te clusters. The ablation time determined the quality of the laser-induced phase transition of $MoTe_2$ from **2H** to **1T′** as well as the subsequent low-temperature transition from **1T′** to $\mathbf{T_d}$. Our research presents a simpler and more reliable method for achieving a controllable and high-quality stable phase transition in 2D TMDCs materials, which has substantial implications for designing devices tailored for specific phase areas, developing low-resistance contact 2D electronics, and exploring their applications in flexible photodetectors and next-generation field-effect transistors.

4. Experimental Section

Multilayer $MoTe_2$ and thin flakes of **h**-BN were mechanically exfoliated from bulk crystals (HQ Graphene). The **h**-BN-encapsulated **2H**-$MoTe_2$ heterostructures were fabricated using polydimethylsiloxane stamps through a dry-transfer technique in the cleanroom.[72] To preserve the high-quality **2H**-$MoTe_2$, the freshly exfoliated multilayer **2H**-$MoTe_2$ was rapidly transferred onto a thermally oxidized 300-nm-thick SiO_2/Si substrate using a 2D material transfer platform. The exfoliated multilayer **h**-BN flakes were precisely transferred onto the multilayer **2H**-$MoTe_2$ using the same 2D material transfer platform, creating a sealed **2H**-$MoTe_2$ to prevent surface oxidation and contamination of **2H**-$MoTe_2$. Laser ablation experiments were conducted using a micro-Raman spectroscopy system (HORIBA HR Evolution) under ambient conditions. A continuous-wave laser beam with a wavelength of 532 nm was focused using a 100× objective lens (numerical aperture = 0.9) for laser ablation. The laser power was set to 25 mW, and the ablation time was set to 1–6 s. The sample was ablated spot by spot with a step size of 0.75 μm, and the total ablation region was $10 \times 10\ \mu m^2$. After laser irradiation, the Raman spectra of the ablated regions were collected on the same Raman spectrometer system using a low laser power of 0.7 mW to prevent heating during Raman characterization. Temperature-dependent Raman spectroscopy was conducted using an optical cryostat (GoGo Instruments, CH600) over a temperature range of 80–300K at 10-K intervals. A multilayer **1T′**-$MoTe_2$ grown by CVD method was used for the reference sample.

Supporting Information

Supporting Information is available from the Wiley Online Library or from the author.

Acknowledgements

H.C. and Y.Y. contributed equally to this work. This work was supported by the National Natural Science Foundation of China (Grant No. 62175253), National Key Research and Development Program of China (Grant Nos. 2023YFF0715902 and 2024YFA1207700), National Natural Science Foundation of China (Grant Nos. 12364012, 62204259, 12074420, U21A20140), CAS Project for Young Scientists in Basic Research (Grant No. YSBR-056), the Strategic Priority Research Program of CAS (Grant No. XDB0670100).

Conflict of Interest

The authors declare no conflict of interest.

Data Availability Statement

The data that support the findings of this study are available from the corresponding author upon reasonable request.

Keywords

$MoTe_2$, laser irradiation, phase transition, Raman spectroscopy

Received: January 22, 2025
Revised: April 20, 2025
Published online:

[1] A. K. Geim, I. V. Grigorieva, *Nature* **2013**, *499*, 419.
[2] Y. Liu, N. O. Weiss, X. Duan, H.-C. Cheng, Y. Huang, X. Duan, *Nat. Rev. Mater.* **2016**, *1*, 16042.
[3] K. Chen, X. Wan, W. Xie, J. Wen, Z. Kang, X. Zeng, H. Chen, J. Xu, *Adv. Mater.* **2015**, *27*, 6431.
[4] Y. Gong, J. Lin, X. Wang, G. Shi, S. Lei, Z. Lin, X. Zou, G. Ye, R. Vajtai, B. I. Yakobson, H. Terrones, M. Terrones, B. K. Tay, J. Lou, S. T. Pantelides, Z. Liu, W. Zhou, P. M. Ajayan, *Nat. Mater.* **2014**, *13*, 1135.
[5] Y. Liu, X. Duan, Y. Huang, X. Duan, *Chem. Soc. Rev.* **2018**, *47*, 6388.
[6] E. Shi, B. Yuan, S. B. Shiring, Y. Gao, Akriti, Y. G., C. Su, M. Lai, P. Yang, J. Kong, B. M. Savoie, Y. Yu, L. Dou, *Nature* **2020**, *580*, 614.
[7] C. Li, K. Liu, H. Yan, L. Zhang, D. Jiang, T. Wen, B. Yue, Y. Wang, *Adv. Mater.* **2024**, *36*, 2407922.
[8] P. K. Sahoo, S. Memaran, Y. Xin, L. Balicas, H. R. Gutiérrez, *Nature* **2018**, *553*, 63.
[9] A. Behranginia, P. Yasaei, A. K. Majee, V. K. Sangwan, F. Long, C. J. Foss, T. Foroozan, S. Fuladi, M. R. Hantehzadeh, R. Shahbazian-Yassar, M. C. Hersam, Z. Aksamija, A. Salehi-Khojin, *Small* **2017**, *13*, 1604301.
[10] P. Yasaei, A. A. Murthy, Y. Xu, R. dos Reis, G. S. Shekhawat, V. P. Dravid, *Adv. Mater.* **2019**, *31*, 1808244.

[11] Y. Ke, J. Guo, D. Kong, J. Wang, G. Kusch, C. Lin, D. Liu, Z. Kuang, D. Qian, F. Zhou, G. Zhang, M. Niu, Y. Cao, R. A. Oliver, D. Dai, Y. Jin, N. Wang, W. Huang, J. Wang, *Adv. Mater.* **2024**, *36*, 2207301.
[12] X. Sun, Y. Liu, J. Shi, C. Si, J. Du, X. Liu, C. Jiang, S. Yang, *Adv. Mater.* **2023**, *35*, 2304171.
[13] M. P. Levendorf, C.-J. Kim, L. Brown, P. Y. Huang, R. W. Havener, D. A. Muller, J. Park, *Nature* **2012**, *488*, 627.
[14] J. Wang, Z. Li, H. Chen, G. Deng, X. Niu, *Nano-Micro Lett.* **2019**, *11*, 48.
[15] Y. Gong, S. Lei, G. Ye, B. Li, Y. He, K. Keyshar, X. Zhang, Q. Wang, J. Lou, Z. Liu, R. Vajtai, W. Zhou, P. M. Ajayan, *Nano Lett.* **2015**, *15*, 6135.
[16] C. Huang, S. Wu, A. M. Sanchez, J. J. P. Peters, R. Beanland, J. S. Ross, P. Rivera, W. Yao, D. H. Cobden, X. Xu, *Nat. Mater.* **2014**, *13*, 1096.
[17] M.-Y. Li, Y. Shi, C.-C. Cheng, L.-S. Lu, Y.-C. Lin, H.-L. Tang, M.-L. Tsai, C.-W. Chu, K.-H. Wei, J.-H. He, W.-H. Chang, K. Suenaga, L.-J. Li, *Science* **2015**, *349*, 524.
[18] M. Liu, J. Gou, Z. Liu, Z. Chen, Y. Ye, J. Xu, X. Xu, D. Zhong, G. Eda, A. T. S. Wee, *Nat. Commun.* **2024**, *15*, 1765.
[19] B. Zheng, C. Ma, D. Li, J. Lan, Z. Zhang, X. Sun, W. Zheng, T. Yang, C. Zhu, G. Ouyang, G. Xu, X. Zhu, X. Wang, A. Pan, *J. Am. Chem. Soc.* **2018**, *140*, 11193.
[20] A. Molina-Sánchez, L. Wirtz, *Phys. Rev. B* **2011**, *84*, 155413.
[21] R. Wu, H. Zhang, H. Ma, B. Zhao, W. Li, Y. Chen, J. Liu, J. Liang, Q. Qin, W. Qi, L. Chen, J. Li, B. Li, X. Duan, *Chem. Rev.* **2024**, *124*, 10112.
[22] Y. Cheon, S. Y. Lim, K. Kim, H. Cheong, *ACS Nano* **2021**, *15*, 2962.
[23] Y. Sun, J. Li, M. Liu, *Matter* **2024**, *7*, 2704.
[24] W. Wan, D. Wickramaratne, P. Dreher, R. Harsh, I. I. Mazin, M. M. Ugeda, *Adv. Mater.* **2022**, *34*, 2200492.
[25] Y. Fang, J. Pan, D. Zhang, D. Wang, H. T. Hirose, T. Terashima, S. Uji, Y. Yuan, W. Li, Z. Tian, J. Xue, Y. Ma, W. Zhao, Q. Xue, G. Mu, H. Zhang, F. Huang, *Adv. Mater.* **2019**, *31*, 1901942.
[26] S. Roy, A. Joseph, X. Zhang, S. Bhattacharyya, A. B. Puthirath, A. Biswas, C. S. Tiwary, R. Vajtai, P. M. Ajayan, *Chem. Rev.* **2024**, *124*, 9376.
[27] D. Tang, M. Dan, Y. Zhang, *Nano Energy* **2022**, *104*, 107888.
[28] W. Yu, Z. Dong, I. Abdelwahab, X. Zhao, J. Shi, Y. Shao, J. Li, X. Hu, R. Li, T. Ma, Z. Wang, Q.-H. Xu, D. Y. Tang, Y. Song, K. P. Loh, *ACS Nano* **2021**, *15*, 18448.
[29] J. Chen, G. Wang, Y. Tang, H. Tian, J. Xu, X. Dai, H. Xu, J. Jia, W. Ho, M. Xie, *ACS Nano* **2017**, *11*, 3282.
[30] Y. Yoo, Z. P. DeGregorio, Y. Su, S. J. Koester, J. E. Johns, *Adv. Mater.* **2017**, *29*, 1605461.
[31] V. K. Nagareddy, T. J. Octon, N. J. Townsend, S. Russo, M. F. Craciun, C. D. Wright, *Adv. Funct. Mater.* **2018**, *28*, 1804434.
[32] Y. Wang, J. Xiao, H. Zhu, Y. Li, Y. Alsaid, K. Y. Fong, Y. Zhou, S. Wang, W. Shi, Y. Wang, A. Zettl, E. J. Reed, X. Zhang, *Nature* **2017**, *550*, 487.
[33] S. Cho, S. Kim, J. H. Kim, J. Zhao, J. Seok, D. H. Keum, J. Baik, D.-H. Choe, K. J. Chang, K. Suenaga, S. W. Kim, Y. H. Lee, H. Yang, *Science* **2015**, *349*, 625.
[34] Y. Tan, F. Luo, M. Zhu, X. Xu, Y. Ye, B. Li, G. Wang, W. Luo, X. Zheng, N. Wu, Y. Yu, S. Qin, X.-A. Zhang, *Nanoscale* **2018**, *10*, 19964.
[35] Y. Tan, F. Luo, M. Zhu, X. Xu, Y. Ye, B. Li, G. Wang, W. Luo, X. Zheng, N. Wu, Y. Yu, S. Qin, X.-A. Zhang, *Nanoscale* **2019**, *11*, 23498.
[36] Y. Lee, S. H. Lee, S. K. Han, J. Park, D. Lee, D. J. Preston, I. S. Kim, M. C. Hersam, Y. Kwon, B. Shong, W.-K. Lee, *ACS Energy Lett.* **2023**, *8*, 4716.
[37] S. Xu, K. Evans-Lutterodt, S. Li, N. L. Williams, B. Hou, J. J. Huang, M. G. Boebinger, S. Lee, M. Wang, A. Singer, P. Guo, D. Y. Qiu, J. J. Cha, *ACS Nano* **2024**, *18*, 17349.
[38] Y. Wang, M. Zhang, Z. Xue, X. Chen, Y. Mei, P. K. Chu, Z. Tian, X. Wu, Z. Di, *Small* **2022**, *18*, 2200913.
[39] Y. Zhu, W. Ai, M. Ye, C. Li, M. Zhou, F. Chu, G. Dong, Y. Zhou, X. Hu, T. Xu, L. Sun, *Nano Today* **2024**, *59*, 102540.
[40] H. Liu, Y. Wu, Z. Wu, S. Liu, V. L. Zhang, T. Yu, *ACS Nano* **2024**, *18*, 2708.
[41] H. Wu, C. He, J. Ge, K. Zhang, Y. Liu, Q. Wang, L. He, W. Zhao, Z. Chen, *Cryst. Growth Des.* **2025**, *25*, 2347.
[42] H. Xu, Y. Xiao, K. A. Elmestekawy, P. Caprioglio, Q. Li, Q. Zhong, Y. Ji, T. Huang, H. Yan, Y. Yang, L. M. Herz, Q. Gong, H. J. Snaith, R. Zhu, L. Zhao, *Energy Environ. Sci.* **2025**, *18*, 246.
[43] H. J. Conley, B. Wang, J. I. Ziegler, R. F. Haglund, Jr., S. T. Pantelides, K. I. Bolotin, *Nano Lett.* **2013**, *13*, 3626.
[44] W. Zhai, J. Qi, C. Xu, B. Chen, Z. Li, Y. Wang, L. Zhai, Y. Yao, S. Li, Q. Zhang, Y. Ge, B. Chi, Y. Ren, Z. Huang, Z. Lai, L. Gu, Y. Zhu, Q. He, H. Zhang, *J. Am. Chem. Soc.* **2023**, *145*, 13444.
[45] P. V. Shinde, M. Hussain, E. Moretti, A. Vomiero, *SusMat* **2024**, *4*, 236.
[46] X. Zhang, X. Qiao, W. Shi, J.-B. Wu, D.-s. Jiang, P. Tan, *Chem. Soc. Rev.* **2015**, *44 9*, 2757.
[47] Q. Song, Q. Tan, X. Zhang, J.-B. Wu, B. Sheng, Y. Wan, X. Wang, L. Dai, P. Tan, *Phys. Rev. B* **2016**, *93*, 115409.
[48] L. Liang, J. Zhang, B. G. Sumpter, Q.-H. Tan, P.-H. Tan, V. Meunier, *ACS Nano* **2017**, *11*, 11777.
[49] H. Kowalczyk, J. Biscaras, N. Pistawala, L. Harnagea, S. Singh, A. Shukla, *ACS Nano* **2023**, *17*, 6708.
[50] Y. Kim, A. Venkatesan, J. Kim, H. Kim, K. Watanabe, T. Taniguchi, D. Whang, G.-H. Kim, *Mater. Sci. Semicond. Process.* **2023**, *153*, 107133.
[51] H. Ryu, Y. Lee, J. H. Jeong, Y. Lee, Y. Cheon, K. Watanabe, T. Taniguchi, K. Kim, H. Cheong, C.-H. Lee, G. H. Lee, *Small* **2023**, *19*, 2205224.
[52] J. Elkins, S. A. Iyengar, O. Verma, H. Shekhar, K. Khodabandehloo, J. Zhou, T. Pieshkov, J. Murukeshan, P. Nordlander, A. Krishnamoorthy, S. Link, R. Vajtai, A. Puthirath, P. M. Ajayan, *Nano Lett.* **2025**, *25*, 2283.
[53] N. Wazir, C. Ding, X. Wang, X. Ye, X. Lingling, T. Lu, L. Wei, B. Zou, R. Liu, *Nanoscale Res. Lett.* **2020**, *15*, 156.
[54] D. Zakhidov, D. A. Rehn, E. J. Reed, A. Salleo, *ACS Nano* **2019**, *14*, 2894.
[55] S. Kang, D. Won, H. Yang, C.-H. Lin, C.-S. Ku, C.-Y. Chiang, S. Kim, S. Cho, *Appl. Surf. Sci.* **2021**, *563*, 150282.
[56] F. Ahmed, C. Rodríguez-Fernández, H. A. Fernandez, Y. Zhang, A. M. Shafi, M. G. Uddin, X. Cui, H. H. Yoon, N. Mehmood, A. C. Liapis, L. Yao, H. Caglayan, Z. Sun, H. Lipsanen, *Adv. Funct. Mater.* **2023**, *33*, 2302051.
[57] H. Zhu, Q. Wang, L. Cheng, R. Addou, J. Kim, M. J. Kim, R. M. Wallace, *ACS Nano* **2017**, *11*, 11005.
[58] X.-B. Liu, S.-Q. Hu, D. Chen, M. Guan, Q. Chen, S. Meng, *Nano Lett.* **2022**, *22*, 4800.
[59] S. Paul, S. Karak, M. Mandal, A. Ram, S. Marik, R. P. Singh, S. Saha, *Phys. Rev. B* **2020**, *102*, 054103.
[60] K. Zhang, C. Bao, Q. Gu, X. Ren, H. Zhang, K. Deng, Y. Wu, Y. Li, J. Feng, S. Zhou, *Nat. Commun.* **2016**, *7*, 13552.
[61] M. Kuiri, S. Das, D. V. S. Muthu, A. Das, A. K. Sood, *Nanoscale* **2020**, *12*, 8371.
[62] I. Jo, M. T. Pettes, J. Kim, K. Watanabe, T. Taniguchi, Z. Yao, L. Shi, *Nano Lett.* **2013**, *13*, 550.
[63] F. J. Manjón, S. Gallego-Parra, P. Rodríguez-Hernández, A. Muñoz, C. Drasar, V. Muñoz-Sanjosé, O. Oeckler, *J. Mater. Chem. C* **2021**, *9*, 6277.
[64] R. N. Zitter, *Surf. Sci.* **1971**, *28*, 335.
[65] H. Ryu, Y. Lee, H.-J. Kim, S.-H. Kang, Y. Kang, K. Kim, J. Kim, B. E. Janicek, K. Watanabe, T. Taniguchi, P. Y. Huang, H. Cheong, I.-H. Jung, K. Kim, Y.-W. Son, G.-H. Lee, *Adv. Funct. Mater.* **2021**, *31*, 2107376.
[66] D. Zakhidov, D. A. Rehn, E. J. Reed, A. Salleo, *ACS Nano* **2020**, *14*, 2894.

[67] F. Ye, A. Islam, Y. Wang, J. Guo, P. X.-L. Feng, *Small* **2023**, *19*, 2205327.
[68] S. S. Awate, K. Xu, J. Liang, B. Katz, R. Muzzio, V. H. Crespi, J. Katoch, S. K. Fullerton-Shirey, *ACS Nano* **2023**, *17*, 22388.
[69] M. Richard-Lacroix, V. Deckert, *Light: Sci. Appl.* **2020**, *9*, 35.
[70] S. Paul, S. Karak, M. Mandal, A. Ram, S. Marik, R. P. Singh, S. Saha, *Phys. Rev. B* **2019**, *102*, 054103.
[71] P. Santra, S. Ghaderzadeh, M. Ghorbani-Asl, H.-P. Komsa, E. Besley, A. V. Krasheninnikov, *npj 2D Mater. Appl.* **2024**, *8*, 33.
[72] P. J. Zomer, M. H. D. Guimarães, J. C. Brant, N. Tombros, B. J. van Wees, *Appl. Phys. Lett.* **2014**, *105*, 013101.